Radio Science

RESEARCH ARTICLE
10.1029/2019RS006826

Key Points:

- Apparent plasma displacements associated with a passing infrasonic wave are similar during all experiments
- *E*-region effects from infrasonic waves include modulation of range and power of HF echoes
- *D*-region absorption is modulated by infrasonic waves

Correspondence to:
J. Mabie,
justin.mabie@noaa.gov

Citation:
Mabie, J., & Bullett, T. (2019). Infrasonic wave-induced variations of ionospheric HF sounding echoes. *Radio Science*, *54*. https://doi.org/10.1029/2019RS006826

Received 3 MAR 2019
Accepted 2 SEP 2019
Accepted article online 5 SEP 2019

Infrasonic Wave-Induced Variations of Ionospheric HF Sounding Echoes

Justin Mabie[1] and **Terence Bullett**[1,2]

[1]Cooperative Institute for Research in Environmental Sciences, University of Colorado Boulder, Boulder, CO, USA, [2]National Centers for Environmental Information, National Oceanic and Atmospheric Administration, Boulder, CO, USA

Abstract We conducted ionospheric observations during several Orbital Corporation International Space Station Resupply missions from the Mid-Atlantic Regional Spaceport at National Aeronautics and Space Administration Wallops Flight Facility in Virginia. These observations were made under different ionospheric and thermospheric conditions using different variations of an experimental sounding mode of the Wallops Vertical Incidence Pulsed Ionospheric Radar. We present an analysis of variations in signal strength (fading), range (signal delay), and echo arrival angle as the rocket-generated High Altitude Acoustic Waves propagate in the thermosphere and through the plasma layers being observed. The results improve our understanding of the effects of infrasonic waves on remote sensing of the ionosphere and on radio wave propagation through the ionosphere and thermosphere.

Plain Language Summary When large rockets are launched, they have been observed to generate infrasonic waves that propagate in the thermosphere (Mabie et al., 2016, https://doi.org/10.1002/2016GL070820). These High Altitude Acoustic Waves can be detected with high-frequency radio sounding techniques as changes in ionospheric plasma motion, radio echo power, and radio wave propagation direction. The presented results improve our understanding of how infrasonic waves in the thermosphere affect the ionosphere, radio remote sensing, and radio wave propagation.

1. Introduction

Infrasonic waves are known to propagate in the thermosphere, but there have been a limited number of observations. These infrasonic waves in the thermosphere are referred to as High Altitude Acoustic Waves (HAAW; Mabie et al., 2016). We have made observations of HAAW with the Vertical Incidence Pulsed Ionospheric Radar (VIPIR) at the National Aeronautics and Space Administration Wallops Flight Facility (WFF) during five rocket launches by measuring ionospheric apparent plasma displacements caused by the HAAW. These HAAW propagate near the adiabatic speed of sound and persist within the ionosphere for several minutes, differing from acoustic gravity waves described by Negrea et al. (2016). This paper analyzes the effects of HAAW on HF radio remote sensing in terms of observed apparent plasma displacements, changes in the direction of radio wave propagation, and modulation of signal strength.

1.1. HAAW Propagation

Neglecting humidity, the adiabatic invariant speed of sound can be expressed as

$$C_s = \sqrt{\gamma R T} \tag{1}$$

where γ is the ratio of specific heats at constant volume and pressure, R is the ideal gas constant, and T is temperature in Kelvin. The HAAW propagates at this speed in the vertical direction. This approximation can fail when the propagation direction is not vertical (Occhipinti et al., 2013), or when the wave is attenuated by the atmosphere (Kherani et al., 2009; Schubert et al., 2005). Altitude dependence of the specific heat ratio (Hines, 1955) is neglected, and a constant value of 1.4 is used. Vertical temperature profiles are given by the NRLMSISE-00 model (Picone et al., 2002). Equation (1) is used to estimate when the HAAW should arrive at *F*-region altitudes to aid in positive detection of the HAAW, and it is used to determine the altitude of the HAAW as a function of time using positive detection as a reference.

1.2. HAAW Detection

Positive identification of HAAW is made based on the magnitude, time, and shape of apparent plasma displacements in the ionosphere (Mabie et al., 2016). Apparent plasma displacements computed by Doppler shift or changes in phase of the received ionospheric echoes (Bianchi & Altadill, 2005) are used to identify when the HAAW arrives at the fixed frequency plasma observation altitude, which is the altitude where the local plasma frequency is equal to the transmitted radio wave frequency. Determination of the speed of apparent plasma displacements includes some uncertainty because it does not account for changes in echo phase not related to Doppler velocity. Also, the observed apparent plasma displacements do not provide clear information on the horizontal properties of the HAAW. Positive identification of rocket-induced HAAW was made during all five experiments when the VIPIR was configured to make these observations.

Some experiments were conducted using a single fixed frequency and some used multiple fixed frequencies. The single fixed frequency observations have better temporal resolution and are considered better for analysis of radio propagation effects. Results that are presented here are from experiments where a single fixed frequency was used.

1.3. Arrival Angle of VIPIR Echoes

The arrival angle of the ionospheric echoes is determined from wave vectors computed by phase interferometry across a 2-D 8-element receive array of 100-m × 100-m dimension. Wave vectors have previously been used to determine ionospheric tilts and to geolocate echoes using ionospheric models (Zabotin et al., 2006) and drive wave vector propagation models (Mitchell et al., 2017). Wave vectors are computed using the techniques described by Mabie et al., 2016.

1.4. Radio Wave Absorption

Absorption of the transmitted VIPIR radio wave is a physical process investigated in this article. We show that changes in absorption can allow for identification of the location of the HAAW at more than one altitude in the thermosphere. Deviative absorption occurs where the radio wave is refracted significantly and nondeviative absorption caused by plasma-neutral collisions occurs when the index of refraction is near unity (Settimi et al., 2014). We discuss variations in deviative absorption near the radio wave reflection point and nondeviative absorption when the radio wave propagates through the *D* region.

The classical approach to evaluating HF radio wave absorption using the Appleton-Hartree Equation makes use of the complex index of refraction, which is dependent on electron density N, electron collision frequency ν, radio wave frequency ω, electron cyclotron frequency ω_{ecf}, and polarization angle θ_P (Kelso, 1964). Future work could leverage modern tools including an improved formulation of the dispersion relation (Zawdie et al., 2017), and computational techniques using modern computers (Scotto & Settimi, 2014).

1.5. Range Delay of Echoes

When the local plasma frequency (ω_N) is close to the VIPIR transmitted radio frequency (ω) the radio wave propagation speed approaches zero and the propagation time increases. This condition occurs near the radio wave reflection altitude where $\omega_N = \omega$. The propagation distance and time where this condition is true depends on the electron density profile. When generating ionograms, echoes are plotted in virtual altitude or range. Virtual range is determined by multiplying the speed of light by propagation time, neglecting retardation of radio wave propagation speed and refraction. Range delay is the resulting difference between measured virtual range and the actual range to the reflection point. Range delay occurs at all altitudes where plasma density is nonzero.

When the electron density gradient is large near the reflection point, the radio wave frequency and the local plasma frequency are only similar over small spatial distances near the reflection point. This means the path length where $\omega_N \approx \omega$ is small and the deviative delay time is relatively small; when the electron density gradient is small near the reflection point, the path length through the region where $\omega_N \approx \omega$ is large and the deviative delay is large.

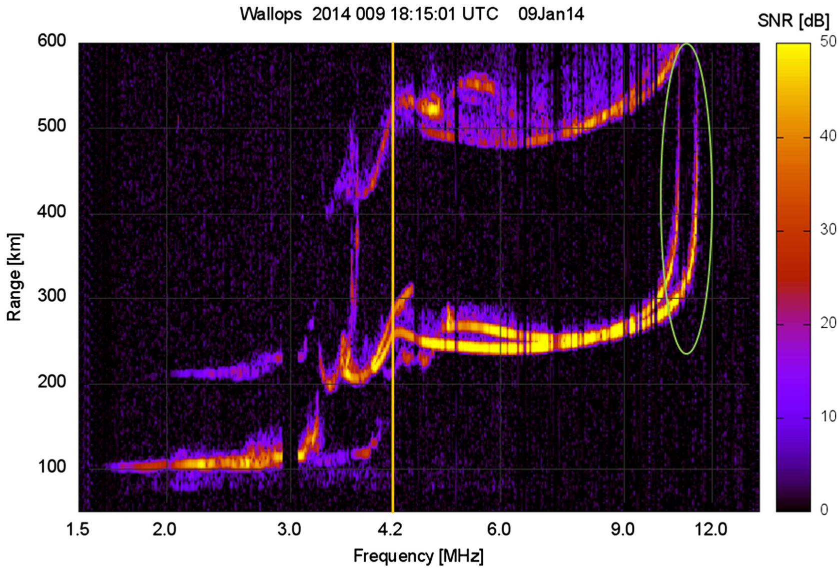

Figure 1. An ionogram showing environmental conditions during the ORB-1 experiment. The 4.2-MHz marker identifies the fixed frequency observation plasma and the *F*2 cusp is identified.

Perhaps the most obvious consequence of this is the presence of the *F*-layer cusps in ionograms like the one shown in Figure 1. Near a layer peak, the density gradient becomes small and radio waves near the critical frequency ω_c experience large delays. These delays manifest as an increase in range, which becomes infinite in the limit where $\omega = \omega_c$ causing formation of the cusp.

1.6. Multipath Effects

Rage delay can also be caused by multipath effects (Malaga & McIntosh, 1978). When a transmitted radio wave is refracted, path length can change and result in a difference in propagation time. For example, a vertically propagating radio wave can be refracted by a horizontal plasma density gradient and a horizontal component to the propagation path can be introduced. In this case the propagation path length and propagation time are increased without any change in the echo reflection altitude.

More than one propagation channel can also exist, and it is possible for there to be more than one propagation path having different path lengths. This condition manifests in ionograms as echoes being observed at multiple ranges.

In this article we first explain how the HAAW are detected and then we analyze the radio propagation effects. These effects will be described in terms of variations in arrival angle, absorption, range delay, and multipath effects. Some special effects from sounding in a layer cusp are identified and discussed.

2. Method

Data collection methods were similar during all five experiments. The VIPIR radar operates with a 10-ms Pulse Repetition Interval and was programmed into "Shuffle Mode," which is one of the many possible modes of operation of the VIPIR invented by the authors (Mabie, 2019). In Shuffle Mode, one or more fixed frequencies are interleaved with the normal sweep frequency transmissions. Shuffle mode allows continuous observations with high temporal resolution at the fixed frequencies while still collecting traditional ionograms and providing ionospheric Electron Density Profiles (EDPs). In this mode, the content of the pulse set is reduced to accommodate a 1-min cadence and each frequency used in the sweep is transmitted only four times.

The sweep frequency observations are processed by a modified version of the Dynasonde software that was designed to work with the reduced pulse set content. The Dynasonde output provides EDPs, estimated true observation heights of HF echoes and specifies other ionospheric properties described by Zabotin et al. (2006). The estimated observation altitudes are obtained from the Dynasonde EDPs which is subject to scaling errors.

By interleaving the fixed frequencies, sweep frequency observations are reduced from 10 to 20ms, but transmission frequencies are still updated every 80ms. A fixed frequency pulse is transmitted every 20ms, and line-of-sight Doppler speeds are computed every 80ms or once per pulse set. This technique avoids having to increase the time it takes to make a full sweep or a need to reduce the number of total observation frequencies. An undesired effect is degradation of the quality of the Dynasonde analysis so that the echo properties are no longer over determined as described by Pitteway and Wright (1992).

The WFF VIPIR radar (WI937) begins sounding at 1,500 kHz due to field site considerations as described by Grubb et al. (2008) and the Dynasonde models lower plasma frequencies to the bottom of the E layer (Zabotin et al., 2006). The upper frequency limit of the observations is 23MHz, but the presented analysis is limited to frequencies at or below f_oF_2. *D*-region plasma frequencies are not reported by Dynasonde.

2.1. Data Processing

The primary processing algorithm uses data from each of eight-dipole receive antennas to find the highest power echo over a defined virtual range interval. From the resulting single in-phase I and quadrature Q values of signal strength, phase change over time is tracked to compute Doppler velocity. Wave vectors are determined by interferometry across the receive array, and variations in range delay are investigated as changes in propagation time or virtual range.

The received echo is interpreted in terms of signal strength V:

$$V = \sqrt{I^2 + Q^2} \tag{2}$$

And power is expressed as a signal to noise ratio:

$$P = 20{*}\log_{10}(V) \tag{3}$$

Phase of the received echo is computed at each receiver using the arctangent of I and Q, and Doppler velocity is computed using change in phase over time for each receive antenna and a single average value is reported for each pulse set. A single wave vector is computed for each pulse using a plane wave approximation applied to a least squares fit of phase values across all eight receive antennas. Virtual range is determined using the propagation time of a wave traveling at the speed of light in a vacuum.

In this article several observed effects are evaluated for each experiment. These include apparent plasma displacements identified as changes in line of sight Doppler velocity, signal fading as variations in received echo power, and arrival angle variations computed from the time series of wave vectors. How each of these are influenced by the respective HAAW are the subject of this article. The analysis is limited to features that are most apparent and is not exhaustive due to the complexity of the data set.

During all presented experiments, the VIPIR operates with a 50-s sweep period followed by a 10-s down time where no observations are made. HAAW arrival times and peak apparent plasma displacements that occur during the down time are interpolated.

3. Observations of Three Rockets

In this article we investigate observations made during the flight of three Antares rockets. All flights were similar International Space Station (ISS) resupply missions. This section provides an explanation of the experimental conditions, VIPIR configuration, and objectives.

3.1. Conditions During ORB-1

The Orbital Corporation Cygnus Commercial Resupply Services (CRS) Orb-1 (ORB-1) ISS resupply Antares rocket was launched 9 January 2014 at 18:07:05 UTC (13:07 local time). The conditions were typical of a

January midday ionosphere with E, $F1$, and $F2$ layers present and an additional cusp below $F1$. Some E layer spread is present within a relatively undisturbed ionosphere. Figure 1 is an ionogram taken 8 min after launch.

The ORB-1 experiment was designed to make a single fixed frequency midday observation at 4,165 kHz, which reflected at an estimated altitude of 156 km. By the time the rocket launched, the $F2$ layer had decayed so that our observation frequency was located within the $F1$ cusp region. This can be seen in Figure 1 with the 4.2 MHz hash being located at the boundary between the $F1$ cusp and the $F2$ trace.

Fixed frequency sounding within a layer cusp is not ideal, but the chosen frequency yielded useful results because the retardation of the radio wave propagation speed has the effect of enhancing some features including apparent plasma displacements and variations in range delay. This effectively improves the VIPIR sensitivity to small plasma displacements at the cost of making the data more difficult to interpret.

3.2. Conditions During OA-5

The Orbital Corporation Cygnus CRS OA-5 (OA-5) ISS resupply Antares rocket was launched on 17 October 2016 at 23:45UTC (7:45 local time). This was an early evening launch with much lower ionospheric plasma densities than during the ORB-1 flight. The ionosphere was characterized by a weaker E layer having some spread and some sporadic-E. A single F-layer trace is present with f_oF_2 near 3.5 MHz. The OA-5 observations were made with a single fixed frequency at 2,661 kHz where the estimated reflection altitude is 245 km.

3.3. Conditions During OA-8

The Orbital Corporation Cygnus CRS OA-8 (OA-8) ISS resupply Antares rocket was launched 12 November 2017 at 12:19:51 UTC (7:19 AM local time). Observations made during the OA-8 flight are a good example of the basic experiment. A single fixed frequency was used to observe the plasma layer at 3,274 kHz, which reflected at an estimated altitude of 190 km.

Ionospheric soundings at the time of the launch showed a weak E layer was followed by a typical $F1$ trace. A highly structured lower $F2$ layer was present and f_oF_2 was near 5 MHz.

4. HAAW Detection

Positive identification of HAAW is made based on the magnitude, time, and shape of apparent plasma displacements in the ionosphere (Mabie et al., 2016). Apparent plasma displacements computed by Doppler shift or changes in phase of the received ionospheric echoes (Bianchi & Altadill, 2005) are used to identify when the HAAW arrives at the altitude where the VIPIR fixed frequency radio pulse is reflected. This is the altitude where the local plasma frequency is equal to the transmitted radio frequency. The shape of these apparent plasma displacements contains some information on the spatial structure of the HAAW.

Plasma displacement calculations do not account for changes in echo phase that are not caused by plasma motion (Bianchi & Altadill, 2005). These echoes are observed in the direction of radio wave propagation, which is approximately vertical, and they do not provide clear information on the horizontal properties of the HAAW. Positive identification of rocket-induced HAAW was made during all experiments when the VIPIR was properly configured to make observations.

The apparent plasma displacements are characterized by an initial upward displacement, followed by a large-amplitude downward displacement, followed by a large-amplitude upward displacement, followed by a relaxation period, which may or may not contain additional HAAW-induced oscillations (Mabie, 2019).

4.1. HAAW Detection and Properties During OA-8

Apparent plasma displacements, variations in absorption, and changes in echolocation are attributed to the rocket-induced HAAW. An example of these observations made during the OA-8 flight can be seen in Figure 2**.** The vertical wavelength of the HAAW at the 190-km estimated observation altitude is computed by taking the time difference between the peak downward and upward apparent plasma displacements as being half the period so that $T = 2 * \Delta t$ and vertical wavelength is

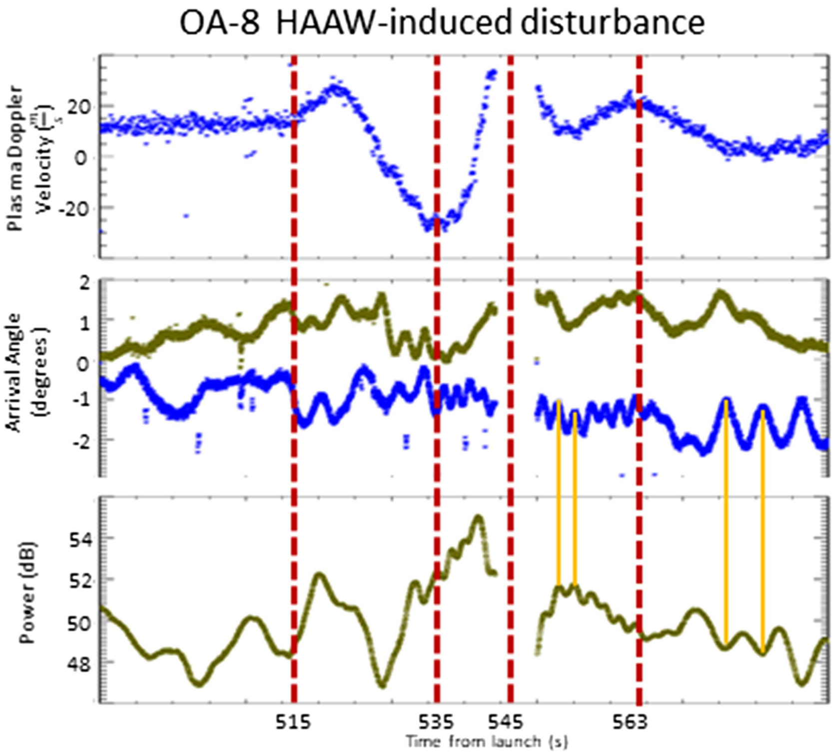

Figure 2. OA-8 observed values for plasma line-of-sight Doppler velocity, arrival angle in the east-west (blue) and north-south (green) directions and power in decibels. Time in seconds from launch (12:19:51 UTC). Fixed frequency observations made at an estimated altitude of 190 km.

$$\lambda = C_s{}^{*}T \tag{4}$$

The downward and upward apparent plasma displacement peaks occur at T+535s and T+545s. With Δt=10 s and $C_s = 506\,\frac{m}{s}$, the HAAW wavelength is $\lambda = 10.1$ km.

Accounting for the 12 s it takes the rocket to clear the launch pad, the HAAW arrived at the fixed frequency observation altitude at T+515s, 23s earlier than predicted using equation (1). Some of this difference may be due to the launch being just after sunrise when temperature values increased between launch time and when the HAAW arrived at the observation altitude. Other potential causes of arrival time error are acceleration of the HAAW that results from atmospheric attenuation (Kherani et al., 2009), and errors in temperature and scaled electron density. Despite the possible sources of error, the propagation times are in generally good agreement with equation (1), these potential errors do not affect the presented results and are not investigated further in this article.

4.2. HAAW Detection and Properties During ORB-1

Observations of arrival angle, power, and plasma velocity during passage of the ORB-1 HAAW are shown in Figure 3. The large-amplitude downward and upward apparent plasma displacement peaks are observed at T+528s and T+535s, so they are separated by 7 s. The estimated fixed frequency observation altitude is 156 km where the sound speed is calculated to be $541\frac{m}{s}$ so that $\lambda = 7.6$km and $T = 14$s.

The HAAW arrives at the fixed frequency observation altitude at T+517s. Equation (1) predicts that it took 477s for the wave to propagate from ground level, and accounting for the 12s it takes the rocket to clear the launch pad, the HAAW arrived 28s later than predicted.

4.3. HAAW Detection and Properties During OA-5

The OA-5 fixed frequency estimated observation altitude was 245 km where the adiabatic sound speed was computed to be $515\frac{m}{s}$. Positive detection of the rocket-induced HAAW is made using Figure 4 where the large-amplitude downward and upward apparent plasma displacement peaks are observed at T+578s

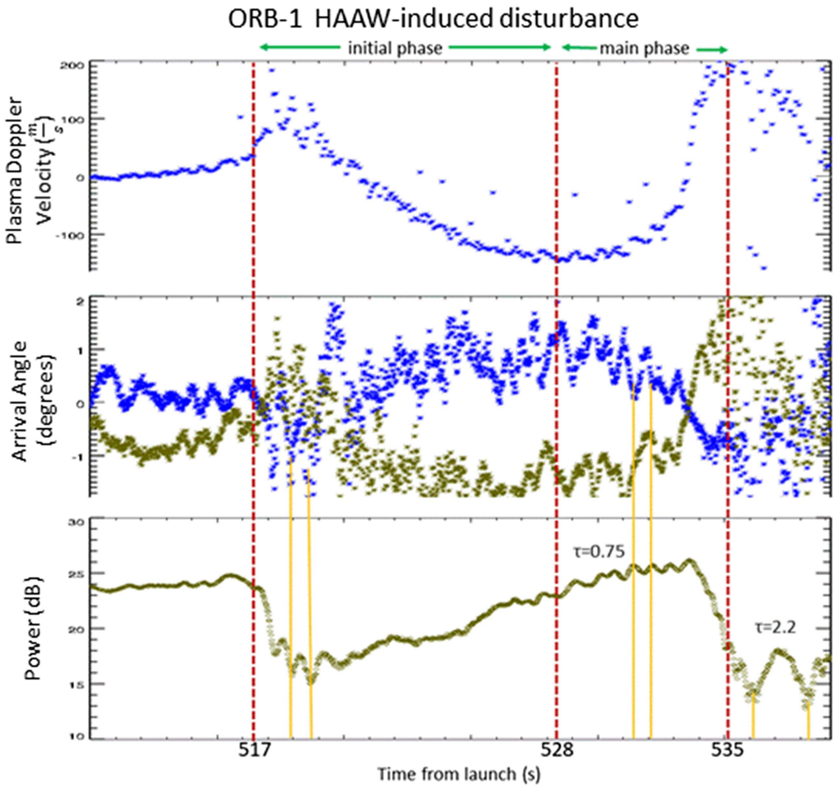

Figure 3. Values of arrival angle, power and plasma velocity observed during the ORB-1 flight. Time in seconds from launch time (18:07:05 UTC). Fixed frequency observations made at an estimated altitude of 156 km.

and *T*+604s. The time between apparent plasma displacement peaks was 25s corresponding to a wavelength of about 26 km.

According to equation (1) it should take the HAAW 648 s to propagate to 245 km. Accounting for the 12 s it takes the rocket to clear the launch pad, predicted arrival time becomes *T*+660s. The large-amplitude downward HAAW-induced apparent plasma displacement peak is observed at *T*+578s. The HAAW arrives at least

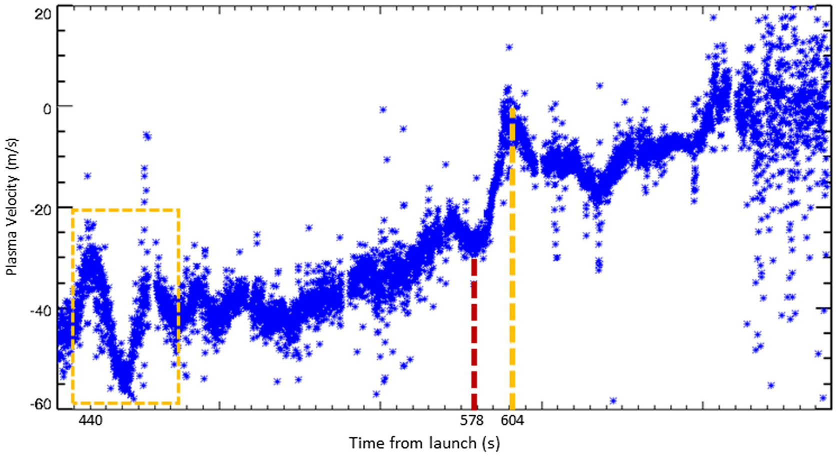

Figure 4. Plasma line-of-sight velocity during the OA-5 experiment. Apparent plasma displacements of near 20m/s not attributed to the High Altitude Acoustic Waves (HAAW) are present along with significantly more structure than during previous experiments. HAAW-induced apparent plasma displacements of less than 20m/s are observed, but a positive identification of the HAAW is still possible. The vertical lines show arrival times for the peak downward and upward apparent plasma displacements. Time in seconds from launch (23:45:35 UTC). Fixed frequency observations made at an estimated altitude of 245 km.

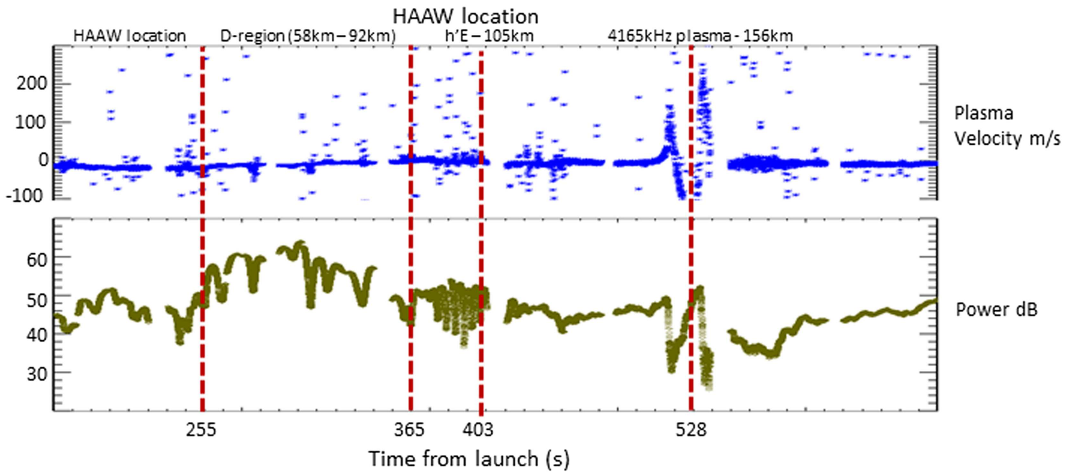

Figure 5. Power and line of sight plasma velocity during the ORB-1 experiment. The HAAW passes through the 4,165-kHz observation plasma near *T*+528s, is within the bottomside *E* region at *T*+393s and is within the *D* region from *T*+255s to *T*+362s. Plasma velocity and power correlate as the HAAW passes through the 4,165-kHz observation plasma. Time is in seconds from launch (18:07:05 UTC). Fixed frequency observations are made at an estimated altitude of 156 km.

82s earlier than predicted, which suggests that it may have traveled faster than the speed of sound. This would imply that the HAAW has undergone attenuation (Schubert et al., 2005). However, the reader is cautioned that early arrival is not conclusive because of uncertainties in the EDP and model temperature profiles.

In Figure 4 there is a plasma disturbance highlighted near the *T*+440s time marker. The nature and propagation speed of this disturbance is not specified, but it is eliminated as being caused by the rocket-induced HAAW because the shape of the apparent plasma displacements differs from other observations of Antares rocket-induced HAAW specified by Mabie (2019). It is also observed too early to be a rocket-induced effect.

5. Special Results From the ORB-1 Observations

The ORB-1 observations were made when the ionosphere was relatively undisturbed so that each plasma layer trace shown in Figure 1 has a clearly defined cusp and little range spread. The 4,165-kHz fixed frequency observations were made within the *F*1 layer cusp. These were midday observations when *D*-region absorption was significant. Because of these factors, deviative radio propagation effects near the reflection point are enhanced and propagation effects that occur away from the reflection point are more prominent than during the other rocket flights.

5.1. Velocity and Power Anomalies During ORB-1

Because of the retardation of the propagation speed of radio waves reflected near a plasma layer cusp, the physical parameters become difficult to interpret. For example, the plot of plasma velocity in Figure 3 shows apparent vertical plasma velocity of more than $200\frac{m}{s}$ compared to the OA-8 apparent plasma displacements closer to $20\frac{m}{s}$. Significant error is introduced by variations in the phase of radio echoes that are caused by cusp effects.

In Figure 5 it can also be seen that abrupt power variations correlate with the HAAW-induced plasma displacements near *T*+528s. Specifically, when the apparent plasma displacements are upward, deviative absorption increases and signal power decreases; when the apparent plasma displacements are downward, deviative absorption decreases and signal power increases.

Prior to HAAW arrival at the 4,165-kHz observation altitude, increased values of power are observed from *T*+255s to *T*+365s and variations in power near *T*+403s are identified. These power variations correspond to when the HAAW is located within the *D* region and in the *E* layer.

The magnitude of changes in radio power associated with the HAAW is not uncommon. However, the observed variations are distinctly different than those observed prior to the HAAW transit through the *D*, *E*, and *F* layers.

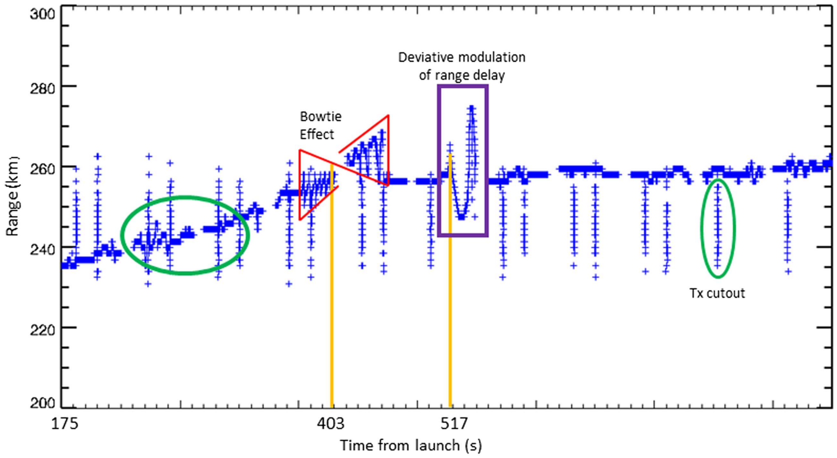

Figure 6. A plot of the range of ionospheric echoes during the ORB-1 flight. Range modulations are highlighted including the bowtie effect when the High Altitude Acoustic Waves (HAAW) is in the E layer and deviative range variations as the HAAW passes the 4,165-kHz observation altitude. The time marker at T+403s denotes the time when h_mE is estimated to be collocated with the HAAW disturbance. Vertical structure in range is the result of loss of signal caused by an impedance mismatch in the Vertical Incidence Pulsed Ionospheric Radar (VIPIR) transmit antenna. Time in seconds from launch time (18:07:05 UTC).

5.2. Range Delays During ORB-1

A range plot of the peak echo power from the ORB-1 4,165-kHz observations is shown in Figure 6. A change in range is observed, which correlates with changes in HAAW-induced line-of-sight plasma velocity peaks near T+517s. These range variations are too large to represent actual plasma displacements and are the result of changes in the radio wave propagation speed near the 4,165-kHz observation altitude.

When the apparent plasma displacements are upward, there is an increase in range; during downward apparent plasma displacements, there is a decrease in range. This is expected from the Appleton-Hartree equation where the local increase in slope of the EDP during downward apparent plasma displacements decreases the spatial distance where $\omega_N \approx \omega$, which decreases range delay; conversely, the local decrease in the slope of the EDP during upward apparent plasma displacements increases the spatial distance where $\omega_N \approx \omega$, which increases range delay.

5.3. Bowtie Effect

There is a sawtooth waveform that appears in the form of an oscillation in range variability with a mean period of 5 s. The midpoint of this feature occurs near T+403 s, 114 s before the HAAW is observed at the 4,165-kHz observation altitude. According to equation (1), this is near the time the HAAW passes h_mE. The sawtooth waveform is characterized by the amplitude of range variations and wave period.

Before the HAAW reaches h_mE, fluctuations over approximately six sawtooth mean wave periods (~30s) show that echo range increases beginning with range variations over an interval of 9km decreasing to 4.5km. At this time the sawtooth wave period is 4 s.

Near the midpoint of the sawtooth wave form, the effect reverses and range decreases over six periods and the amplitude of range varies over 6 km increasing to 15km. At this time, the sawtooth wave period is 6 s.

The observed sawtooth wave has the shape of a bowtie and is henceforth referred to as the “bowtie effect.” Before the HAAW reaches h_mE, the sawtooth wave has a period of 4s, positive change in Doppler velocity, and decreasing amplitude. After the HAAW passes h_mE, the sawtooth wave has a period of 6s, negative change in Doppler velocity, and increasing amplitude.

Figure 7 is a contour plot of received power at the time the bowtie effect is observed with a plot of peak power overlaid. The red lines represent progression of the peak echo strength with respect to the vertical (yellow lines). The overlaid peak power plot in Figure 7 shows that the received power is modulated phase coherent with the sawtooth waveform when the HAAW is below h_mE. After the midpoint of the bowtie effect when the HAAW is located above h_mE, the received power is not modulated significantly.

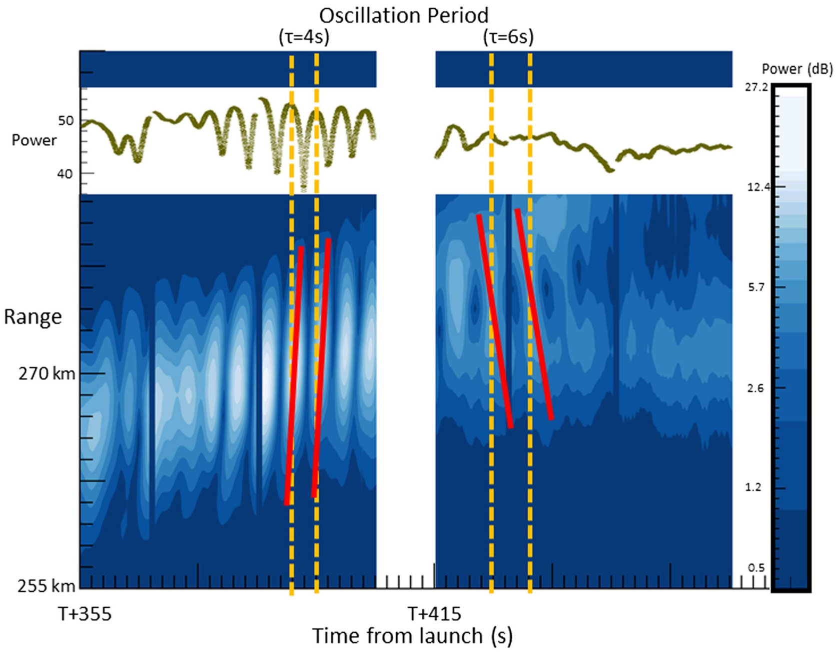

Figure 7. The bowtie effect during the ORB-1 flight. An upward sawtooth progression occurs during the first half of the feature and a downward sawtooth progression during the second half. The period is about 4s during the first half of the feature and 6s during the second half. The center of the bowtie effect occurs near the time the High Altitude Acoustic Waves (HAAW) passes h_mE. Peak power is modulated below h_mE and is phase coherent with the sawtooth wave. After the HAAW passes h_mE, power is fairly constant, while a sawtooth wave is still present. Time in seconds from launch time (18:07:05 UTC). During this observation, the HAAW is located near $h'E$, which is estimated to be at 103 km.

The VIPIR range gate sampling is 1.5 km, and the ORB-1 HAAW signature was determined to have a 7.6-km vertical extent. This makes it instructive to plot how the received power varies in altitude. In Figure 8 power values from 240- to 280-km range are displayed. Markers show when the HAAW is estimated to be near the bottom of the *D* region (58 km), near $h'E$ (90km), near h_mE (103km), and near the 4,165-kHz observation altitude.

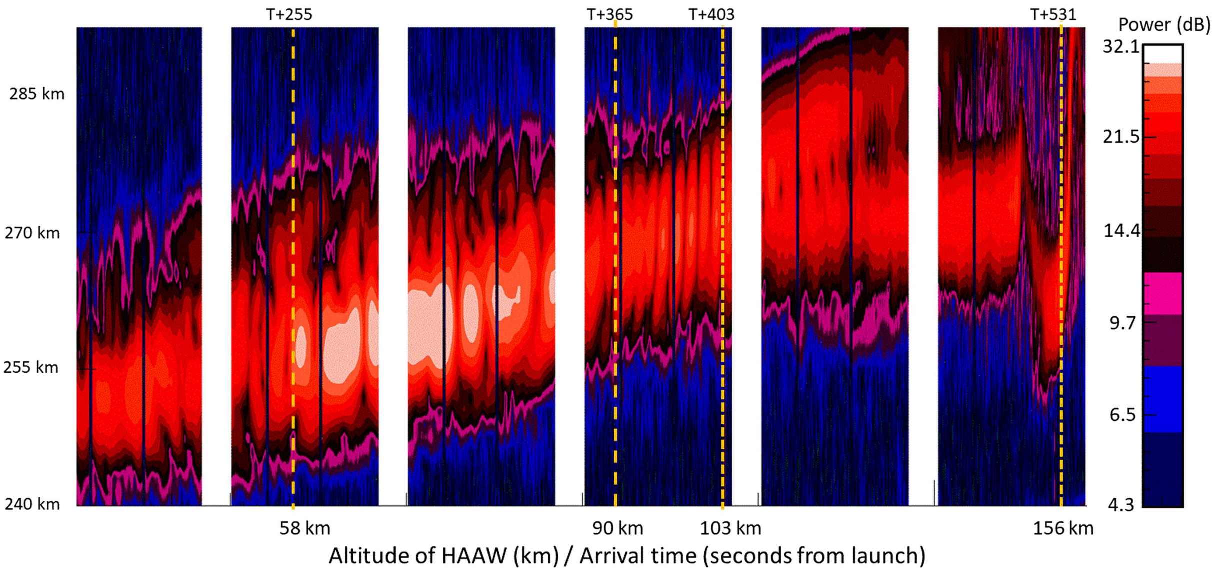

Figure 8. A contour plot of power over time and range while the ORB-1 High Altitude Acoustic Waves (HAAW) propagates within the ionosphere. Received power increase and range spread is observed, while the HAAW is within the *D* region, range modulation and signal bifurcation occur when the HAAW is in the *E* region, and a sharp range modulation occurs as the HAAW passes the 4,165-kHz observation altitude. Time in seconds from launch time (18:07:05 UTC).

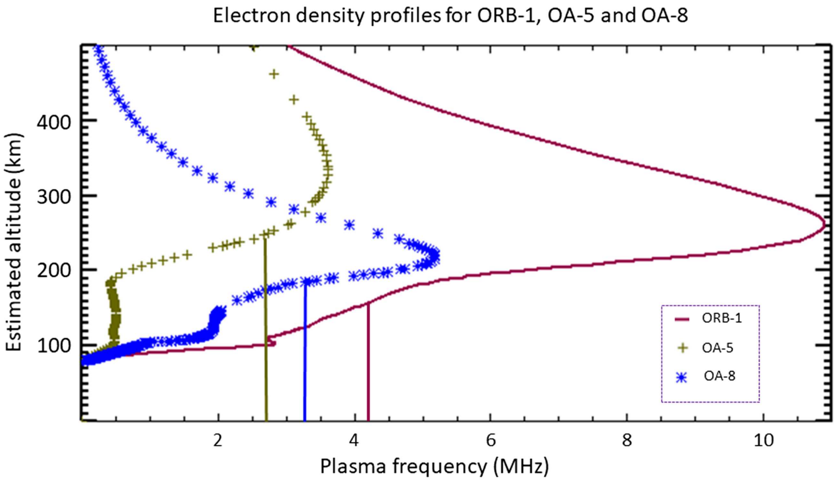

Figure 9. Plot of electron density profiles during all three rocket flights. Frequency and estimated altitude of fixed frequency observations are marked by the vertical lines.

The range-time-intensity patterns in Figure 8 are atypical for *F*-layer reflections, even those subject to multipath in the ionogram cusp region. In particular, the time period of amplitude variations is relatively rapid at about 5 s. Since this effect appears as the HAAW propagates through the *E* layer, and the observation radio wave is penetrating that same *E*-layer ionization, we attribute the bowtie effect to structure in the *E* region, where greater and lesser ray path integrated electron concentrations, caused by the HAAW, create phase advances and retardations to the incident HF wavefront. These phase changes cause the radio wave to emerge on the topside of the *E* layer with a spatially modulated phase front, which then develops into an amplitude-modulated interference pattern as the wave propagates to the *F* layer. This pattern changes in time as the plasma changes. This is similar to the phase screen model of amplitude scintillation under weak scattering conditions (Rino, 1979).

5.4. *D*-Region Absorption

One unique result of this experiment is that it allows for identification of the lower *D*-region boundary. In the *D* region there is little refraction of HF radio waves, but the product of the electron number density and the collision frequency is large. Based on the NRLMSISE-00 modeled atmospheric conditions during both launches, the Appleton-Hartree equation predicts that *D*-region absorption (Settimi et al., 2014) decreases with increasing collision frequency. Because the HAAW is characterized as an overpressure anomaly, the increased neutral atmosphere pressure corresponds with an increased collision frequency and decreased *D*-region absorption.

In Figure 8 there is an increase in received power and range spread before the HAAW reaches the bottom of the *E* region (*h′E*). This enhancement of received power is attributed to a decrease in absorption, while the HAAW is propagating through the part of the atmosphere where *D*-region absorption occurs.

We locate the lower boundary of the *D* region by identifying the time when the received power enhancement begins and compute the HAAW location using equation (1). We conclude that the lower boundary of the *D* region is near 58-km altitude.

6. HAAW-Induced Variations in Arrival Angle

Some HAAW-induced variations in arrival angle are observed. In Figure 3 there are variations in arrival angle that are phase coherent with received power. There is also a long-period variation in arrival angle that begins at the same time as the first upward HAAW-induced apparent plasma displacement is maximum near the time of the large-amplitude downward apparent plasma displacement peak and ends near the time of the large-amplitude upward apparent plasma displacement peak. This arrival angle feature could provide some information on the spatial structure of the HAAW, including the wave's horizontal extent.

7. Conclusions

During five Antares rocket flights, we performed experiments that detected rocket-induced infrasonic waves in the thermosphere. During all flights, the rocket type, payload, and destination were similar. We were able to consistently identify HAAW-induced apparent plasma displacements in the *F*-region ionosphere. The estimated altitude, frequency, and location within the ionospheric EDP is shown in Figure 9. The form of the observed apparent plasma displacements is similar in all cases, independent of time of day and season. The HAAW is also found to modulate electron density profiles in the *E* and *F* layers and collision frequencies in the *D* layer.

In all instances the HAAW-induced apparent plasma displacements are characterized by an initial upward shift in plasma velocity, followed by a large-amplitude downward shift in plasma velocity, followed by a large-amplitude upward shift in plasma velocity, followed by a relaxation period, which may or may not contain additional oscillations.

It is by chance that in ORB1 the fixed frequency was near the *F*1 layer peak plasma frequency and showed large changes in ionogram virtual range. For other experiments, the fixed frequency was not near the ionogram cusp, represented by a change in slope of the EDP in Figure 9.

These HAAW observations afford the opportunity for further investigation of propagation speeds and the precise nature of the ionosphere-thermosphere coupling processes. This work can be expanded for investigation of HAAW generated by other source types like earthquakes once new automated modes of VIPIR operation are developed.

Acknowledgments

AcknowledgementsThis work is supported by the National Aeronautics and Space Administration grant NNX09AI76G. The authors thank Tatiana Sazonova for her support and help in drafting this manuscript. Data used in support of this work can be obtained from the NOAA National Centers for Environmental Information.

References

Bianchi, C., & Altadill, D. (2005). Ionospheric Doppler measurements by means of HF-radar techniques. *Annals of Geophysics*, *48*, 6. https://doi.org/10.4401/ag-3248

Grubb, R. N., Livingston, R., & Bullett, T. W. (2008). A new general purpose high performance HF Radar. In *Proceedings of URSI General Assembly 2008*. Chicago, IL: International Union of Radio Science, GH4, 130–137. http://www.ursi.org/proceedings/procGA08/papers/GHp4.pdf

Hines, C. O. (1955). Hydromagnetic resonance in ionospheric waves. *Journal of Atmospheric and Terrestrial Physics*, *7*, 14–30. https://doi.org/10.1016/0021-9169(55)90103-3

Kelso, J. M. (1964). *Radio Ray Propagation in the Ionosphere*, *Electronic Science Series*, (). McGraw-Hill: Library of Congress. Catalog Card Number 63-15022

Kherani, E. A., Lognonne, P., Kamath, N., Crespon, F., & Garcia, R. (2009). Response of the ionosphere to the seismic triggered acoustic waves: electron density and electromagnetic fluctuations. *Geophysical Journal International*, *176*, 1–13. https://doi.org/10.1111/j.1365-246X.2008.03818.x

Mabie, J., Bullett, T., Moore, P., & Vieira, G. (2016). Identification of rocket-induced acoustic waves in the ionosphere. *Geophysical Research Letters*, *43*, 11,024–11,029. https://doi.org/10.1002/2016GL070820

Mabie, J. (2019). Infrasound induced plasma perturbations associated with geomagnetic pulsations. *Russian Journal of Earth Sciences*, *19*, ES3002. https://doi.org/10.2205/2019ES000661

Malaga, A., & McIntosh, R. E. (1978). Delay and Doppler power spectra of a fading ionospheric reflection channel. *Radio Science*, *13*(5), 859–872. https://doi.org/10.1029/RS013i005p00859

Mitchell, C. N., Rankov, N. R., Bust, G. S., Miller, E., Gaussiran, T., Calfas, R., et al. (2017). Ionospheric data assimilation applied to HF geolocation in the presence of traveling ionospheric disturbances. *Radio Science*, *52*, 829–840. https://doi.org/10.1002/2016RS006187

Negrea, C., Zabotin, N., Bullett, T., Fuller-Rowell, T., Fang, T.-W., & Codrescu, M. (2016). Characteristics of acoustic gravity waves obtained from Dynasonde data. *Journal of Geophysical Research: Space Physics*, *121*, 3665–3680. https://doi.org/10.1002/2016JA022495

Occhipinti, G., Rolland, L., Lognonne, P., & Watada, S. (2013). From Sumatra 2004 to Tohoku-Oki 2011: The systematic GPS detection of the ionospheric signature induced by tsunamigenic earthquakes. *Journal of Geophysical Research: Space Physics*, *118*, 3626–3636. https://doi.org/10.1002/jgra.50322

Picone, J. M., Hedin, A. E., Drob, D. P., & Aikin, A. C. (2002). NRLMSISE-00 empirical model of the atmosphere: Statistical comparison and scientific issues. *Journal of Geophysical Research*, *107*(A12), 1468. https://doi.org/10.1029/2002JA009430

Pitteway, M. L. V., & Wright, J. W. (1992). Toward and optimum receiving array and pulse set for dynasonde. *Radio Science*, *27*(4), 481–490. https://doi.org/10.1029/92RS00269

Rino, C. L. (1979). A power law phase screen model for ionospheric scintillation: 1. Weak scatter. *Radio Science*, *14*(6), 1135–1145. https://doi.org/10.1029/RS014i006p01135

Schubert, G., Hickey, M. P., & Waltersheid, R. L. (2005). Physical processes in acoustic wave heating of the thermosphere. *Journal of Geophysical Research*, *110*, D07106. https://doi.org/10.1029/2004JD005488.46

Scotto, C., & Settimi, A. (2014). The calculation of ionospheric absorption with modern computers. *Advances in Space Research*, *54*, 1642–1650. https://doi.org/10.1016/j.asr.2014.06.017

Settimi, A., Ippolito, A., Cesaroni, C., & Scotto, C. (2014). Scientific review on the ionospheric absorption and research prospects of a complex eikonal model for one-layer ionosphere. *International Geophysical Journal*, *2014*, 657434. https://doi.org/10.1155/2014/657434

Zabotin, N. A., Wright, J. W., & Zhbankov, G. A. (2006). NeXtYZ: Three-dimensional electron density inversion for dynasonde ionograms. *Radio Science*, *41*, RS6S32. https://doi.org/10.1029/2005RS003352

Zawdie, K. A., Drob, D. P., Siskind, D. E., & Coker, C. (2017). Calculating the absorption of HF radio waves in the ionosphere. *Radio Science*, *52*, 767–783. https://doi.org/10.1002/2017RS006256